

Nanoscale

Accepted Manuscript

This article can be cited before page numbers have been issued, to do this please use: J. Deng, C. Liu and M. J. Madou, *Nanoscale*, 2020, DOI: 10.1039/D0NR00031K.



This is an Accepted Manuscript, which has been through the Royal Society of Chemistry peer review process and has been accepted for publication.

Accepted Manuscripts are published online shortly after acceptance, before technical editing, formatting and proof reading. Using this free service, authors can make their results available to the community, in citable form, before we publish the edited article. We will replace this Accepted Manuscript with the edited and formatted Advance Article as soon as it is available.

You can find more information about Accepted Manuscripts in the [Information for Authors](#).

Please note that technical editing may introduce minor changes to the text and/or graphics, which may alter content. The journal's standard [Terms & Conditions](#) and the [Ethical guidelines](#) still apply. In no event shall the Royal Society of Chemistry be held responsible for any errors or omissions in this Accepted Manuscript or any consequences arising from the use of any information it contains.

Ultra-thin carbon nanofibers based on graphitization of near-field electrospun polyacrylonitrile

Jufeng Deng^{1,2}, Chong Liu¹, Marc Madou^{2,3}

¹School of Mechanical Engineering, Dalian University of Technology, China, 116023

²Mechanical and Aerospace Engineering, University of California, Irvine, USA, 92617

³School of Engineering and Science, Tecnologico de Monterrey, Mexico, 64849

Abstract: A novel manufacturing means for arrays of carbon fibers with diameters of less than 10 nm has been developed. The method improves dramatically upon the state of the art of making carbon fibers by pyrolysis of near field electrospun (NFES) polyacrylonitrile (PAN) fibers. The conductive nature of the PAN ink, a touch and retract mode of the droplet at the ejector needle tip and a rotating drum for jet initiation as well as a tight control of the ink flow and droplet shape with a porous paper enable continuous near field electrospinning at an ultra-low voltage of 35V - far below current low-voltage NFES practice. By pyrolyzing the thus obtained thinner PAN nanofibers on carbon scaffolds a dramatic further shrinkage of the diameter leads to ultrathin carbon nanofibers e.g. from a ~245nm polymer fiber to a ~5nm carbon fiber i.e. a 4900 % reduction in fiber diameter. To increase and survive the thinning during the pyrolysis process, PAN stabilization at a relatively low temperature (115 °C) and carbon support scaffolds are implemented to provide just the right amount of tension of the suspended polymer nanofibers. A small inter-fiber spacing (< 8 μm) of the ultrathin carbon fibers in an array is achieved by simultaneously controlling the linear speed of the spinneret and the rotational speed of the collector. In one application, we demonstrate aligned ultra-thin carbon fibers freely suspended and in good ohmic contact with carbon scaffolds on a silicon substrate.

Keywords: Manufacturing, ultrathin carbon fiber, electrospinning, polymeric nanofibers, microstructure.

New methods to fabricate carbon nanofibers have sparked a wave of research interest into their potential applications such as in thermal-management¹, oxygen reduction catalysts² and as components for nanoelectronics and nanophotonics³. Ultrathin patterned carbon fibers are expected to exhibit much enhanced electrical, thermal and mechanical performance and to enable the development of multifunctional devices. Typically, such fibers are produced either by pyrolyzing fibers spun in far field electrospinning from polymeric precursors such as polyacrylonitrile (PAN)⁴, and SU-8⁵ or by chemical vapor deposition (CVD)⁶. Using pyrolysis methods, carbon fibers with diameters ranging from 100 nm to 1000 nm are typically obtained but the fibers are randomly deposited in mats⁷⁻⁸. Thinner carbon nanofibers -in the few nanometer range -have been fabricated using CVD but this results again in large area mats of intertwined carbon fibers.⁹ Patterning of plasma-enhanced CVD fibers,¹⁰ leads to spatial control but unfortunately this is accompanied by an increase in fiber diameter. This has led to extensive research into near-field electrospinning (NFES) that enables the controlled deposition of polymer nanofibers and, when followed by pyrolysis, results into well controlled arrays of carbon nanofibers.¹¹ Traditionally, NFES leads to thicker fibers (> 1 μm) than far field electrospinning,

and one key desirable next breakthrough in NFES is to thus to produce thin polymer fibers (~ 100 -200 nm range) that upon pyrolysis result in yet thinner carbon fibers. Using a modified near-field electrospinning method, Bisht et al.¹², for the case of a highly viscoelastic polyethylene oxide (PEO) ink, demonstrated that lower voltages result into thinner polymer fibers suggesting the possibility of achieving nanoscale manufacturing in NFES. Unfortunately, PEO is a low carbon content polymer that cannot be converted to carbon through pyrolysis.¹² Therefore, a key impediment for the fabrication of thin pyrolyzable polymer nanofibers like PAN is the challenge of continuous electrospinning carbon rich fibers at ultralow voltages. Another challenge is to increase the amount of thinning without breaking of the nanofibers during the conversion of the polymeric precursor to carbon. Over the last few decades PAN stabilization was typically carried out in air at 200 - 300 °C before carbonization at > 800 °C in an inert atmosphere.¹³⁻¹⁶ Although this process leads to significant weight loss and shrinkage,¹⁷ resulting in the decrease of fiber diameter by about 50%, significantly less research has been carried out on how to increase shrinkage further up to 80%.¹⁸

In this work, we demonstrate a novel near-field electrospinning method for making thinner PAN polymeric nanofibers by working at ultra-low voltages. The subsequent pyrolysis of these thinner polymer fibers in a new carbonization procedure leads to ultrafine carbon fibers (as thin as 4 nm). The advances that allow for the desired ultralow voltage operation are a highly conductive polymer ink used in an innovative contact and retract method between liquid body at the tip of the needle and a rotating drum in combination with a tight control of the volume of the fluid body at the needle tip with a porous paper and very low ink flow rates. The dramatic further shrinkage of the thinner polymer nanofibers during pyrolysis depends on the stress management method in the nanofiber and involves a carbon scaffold, lower stabilization temperature and a higher pyrolysis rate, all contributing to maximize the amount of weight loss and diameter shrinkage turning thinner patterned polymer nanofibers into ultrathin carbon nanofibers.

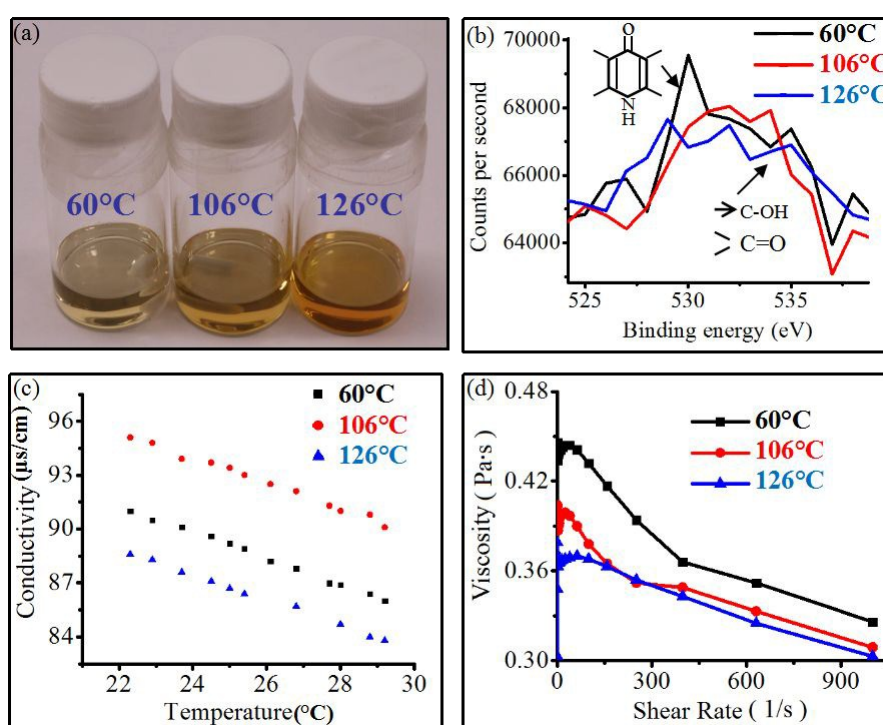


Figure 1. Evaluation of the PAN/DMF Ink. (a) Photograph of PAN/DMF solution after different heat treatments resulting in an apparent color change. (b) X-ray photoelectron spectra of O 1s in the heated PAN/DMF solution oxidized at 60°C, 106°C, and 126°C respectively. (c) Conductivity vs measurement temperature plot for oxidized PAN ink in the Figure (b). (d) Viscosity as a function of shear rate and oxidization temperature (carried out at room temperature).

View Article Online
DOI: 10.1039/D0NR00031K

To attain consistent small polymer fiber diameters at the very lowest applied voltages in near field electrospinning, the fiber jet emanating from the droplet meniscus at the ejector needle tip must be consistently initiated and maintained. To attain this goal, one important procedure concerns the protocol for the dissolution of PAN in N,N-Dimethylformamide (DMF) to make the ink. The usual protocol for preparing a PAN/DMF solution consists of mixing PAN with DMF and stirring at a constant temperature of 60 °C until a homogeneous solution is obtained.¹⁹ Here, we ramp the temperature up to 106 °C at 1.7 °C/hour and then keep it at 75 °C for 48 hours, this heat treatment is accompanied by a slight color change from light yellow to dark brown [see Figure 1(a)]. The binding energies of oxidized PAN ink at 60 °C in the X-ray photoelectron spectra of O 1s in Figure 1(b) reveal that, the lower bonding energy component corresponds to acridone type carbonyl and the higher energy one is assigned to normal carbonyl and alcohol groups.²⁰ This confirms that the (C=O) polar groups from the DMF solvent are available for dipole-dipole interaction with the nitrile groups of the PAN, resulting in low electrostatic repulsion between the CN groups as they are shielded by solvent molecules. Upon increasing the oxidation temperature from 60 °C to 106 °C -which corresponds to the temperature that yields the highest conductivity in Figure 1(c)- the comparable intensity in the bonding energy in Figure 1(b) display an increase in the normal carbonyl and alcohol group peaks. The decrease of the solvent entropy with temperature reduces the solvent diffusion and penetration of the free molecules in the PAN chains, resulting in the enhancement of the dipole-dipole interactions between CN and DMF molecules.²¹ Combined with the lowest intensity at 126 °C in Figure 1(b), the conductivity of the PAN/DMF solution in Figure 1(c) increases with decreasing temperature from 126 °C to 106 °C.

Importantly, the ink aging process is also accompanied by the reduction of the coil dimension of the polymer, due to the conformational change of the PAN chain from a planar zigzag structure to a helix structure.²¹ As expected, the viscosity of a dilute solution is an indirect indication of the hydrodynamic volume of a single polymer coil and decreases with its reduction. The viscosity in Figure 1(d) indeed noticeably decreases, particularly at 106 °C and 126 °C, for which similar results with respect to temperature pretreatment are obtained.²¹

The ink preparation protocol changes introduced here dramatically helped the initiation of the jetting by a touch and retract mode, and in sustaining the liquid bridge between the needle and the rotating drum formed this way (see below). With the proper ink pre-treatment, a sustainable fiber ejection at 500V and below becomes possible (see Figure 2 and Figure 4), indicating that the heat treatment changes the ink in a substantial way making the ultrathin fiber manufacturing process possible.

In near field electrospinning (NFES), jet initiation is normally prevented by the lower strength of the working electric field because the electrostatic force is not sufficient to overcome the surface tension of the polymer droplet at the tip of the ejector needle. To initiate a nano-jet in NFES, an instability has to be introduced onto the droplet surface. This can be done, for example, by touching the droplet with a glass microprobe tip, that causes a local, very high local electric

field distortion that is sufficient to overcome the surface tension and gives rise to the formation of a Taylor cone and the initiation of a PEO jet at a low-voltage (200V).¹² Similarly, for PAN jet initiation at low voltages, a large enough electrical stress on the liquid surface has to be induced.

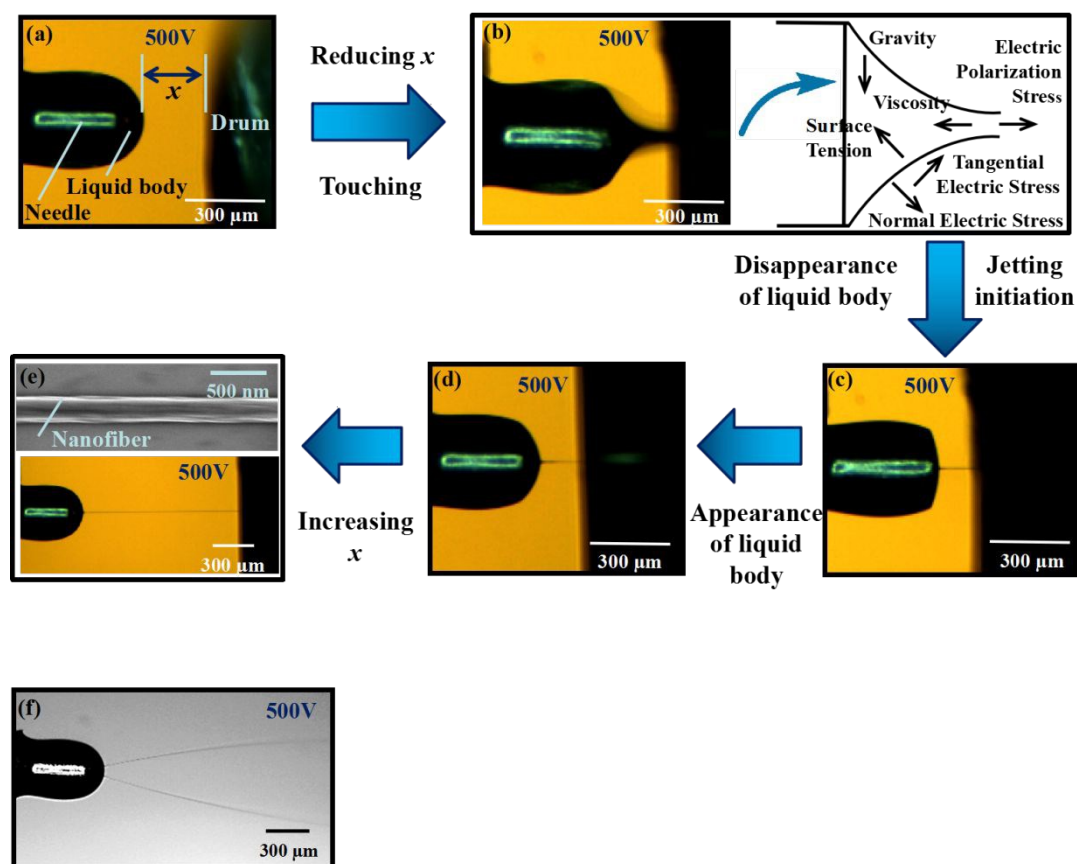


Figure 2. Schematic of the low-voltage near-field electrospinning process. (a-e) Jetting initiation at 500V. A change in flow rate between 1 and 0 nl/min does not affect the formation of the jet. (f), Two continuous jets emanating from the nozzle at 500V.

We use a home-built near-field electrospinning (NFES) set-up to initiate jetting of the polymer nanofibers from the modified PAN/DMF ink. In Figure 2(a)-2(e) we illustrate an experiment where we apply 500 volts (V) between the needle and the rotating drum. The needle is then brought closer to the rotating drum till it touches the drum and the shape of the liquid surface transforms from a hemispherical shape into a conical shape. The movement of the needle towards the drum (smaller and smaller x) causes a rapid increase in the x component of the applied electric field E_x according to $E_x = V_{\text{applied}} / x$ where V_{applied} and x are, respectively, the applied voltage and distance between the needle and the droplet. In the physical contact that follows, the liquid surface is deformed from concave into a conical shape [see Figure 2(b)] and this increases the average contribution of the normal component in the direction of the main electric field over the droplet surface. Upon transition from a conical shape to one point in Figure 2(c), the corresponding normal electrical stress on the liquid surface becomes large enough to counter balance the surface tension stress leading to jet initiation. After the formation of the jet, the very slow outflow of the liquid inside the needle causes the liquid at the tip to transform back into a cone as seen in Figure 2(d), next we increase the distance x to reach $x=1.85\text{mm}$ in Figure 2(e), this results in decreasing

the normal electrical stress but a continuous jetting state is maintained and polymer nanofibers with a diameter of ~240nm result. This behavior can be explained by the high conductivity of the PAN/DMF ink which corresponds to a higher charge density and an increasing electrical stress. When using a PAN ink heated to either 60 °C or 130°C, jetting initiation at 500V is not achieved in the same touching procedure illustrated in Figure 2(a) ~ Figure 2(e). In addition, if no touching between the liquid body at the tip of the needle and the drum to change the shape of the liquid body takes place, the jet does not initiate even at a higher voltage $V_{\text{applied}}=1500\text{V}$ and $x=1.85\text{mm}$. Thus, we attribute the jetting initiation to the increase of the normal electrical stress and the relatively higher conductivity of the inks pretreated at 106°C.

Regarding the minimum voltage required to obtain a stable jet, the appearance of multi-jets should be avoided.²² As shown in Figure 2(f) when the drum surface is rough at voltage down to 500 volts, two jets are initiated. The one-jet to two-jet transition occurs by increasing the contacting points between the hemispherical droplets and drum. This is different from the previous mechanism, which only increases the normal electrical field intensity by increasing the applied voltage so as to maintain multi-mode jetting.²²

After stable jetting has been achieved, the governing equation of the jetting velocity v for the steady-state flow is introduced as follows²³:

$$v = \frac{Q}{h^2} \quad (1)$$

Where Q is a volume flow rate and h is the cross-sectional radius.

With a surface charge density σ , the conservation of charge dictates that²³:

$$\sigma h v + \frac{K^*}{2} h^2 E = I \quad (2)$$

where $K^*=K[r_0^3\rho/(\gamma\beta)]^{1/2}$ with $\beta=\epsilon^{3/2}-1$ is the dimensionless conductivity of the fluid, K is electric conductivity, r_0 determined by the nozzle radius is a length scale,²³ ρ is the fluid density, γ is the fluid surface tension, ϵ is the dielectric constants, E is the electric field strength and I is the total current in the electrified jet.

Therefore, from Equation (1) and (2) we obtain:

$$\frac{\sigma Q}{h} + \frac{K^*}{2} h^2 E = I \quad \left(\frac{\sigma}{h} + \frac{K^* h^2 E}{2Q} = \frac{I}{Q} \right) \quad (3)$$

In near-field electrospinning, the electrical forces imposed on the jet far overweight the other forces and therefore, the dominant remaining terms in the Navier-Stokes equation is the balance between inertia and tangential electric stress²³:

$$\frac{d}{dx} \left(\frac{v^2}{2} \right) = \frac{2\sigma E}{h\sqrt{\beta}} \quad (4)$$

From Equation 3 it follows that when that $h^2/Q \rightarrow 0$ as $h \rightarrow 0$, it leads to the asymptotic disappearance of advection-dominated current or ($Q\sigma/h \approx I$). It should be noted that the reduction of the jet diameter in this paper is achieved performed under the condition that the flow velocity is asymptotically approaching zero in our work (see below). But, for all this, h^2/Q has to be retained in Equation (3) to ensure charge conservation. By combining Equation (3) and (4), the final

expressions for the cross-sectional fiber radius h is given as:

View Article Online
DOI: 10.1039/D0NR00031K

$$h = \text{InverseFunction} \left\{ \left[-\frac{E^2 K^2 I n x}{8I^3} + \frac{E^2 K^2 \ln(-2I + EKx^2)}{16I^3} + \frac{1}{8Ix^4} + \frac{EK}{8I^2 x^2} \right] \left[\frac{Ex}{2Q^3 \sqrt{\beta}} + C_1 \right] \right\} \quad (5)$$

where C_1 is constant.

Replacing the cross-sectional radius h in Equation (1), the following jet velocity v Equation is obtained :

$$v = \frac{Q}{\left\{ \text{InverseFunction} \left\{ \left[-\frac{E^2 K^2 I n x}{8I^3} + \frac{E^2 K^2 \ln(-2I + EKx^2)}{16I^3} + \frac{1}{8Ix^4} + \frac{EK}{8I^2 x^2} \right] \left[\frac{Ex}{2Q^3 \sqrt{\beta}} + C_1 \right] \right\} \right\}^2} \quad (6)$$

As mentioned above, jetting initiates when the normal electrical stress on the liquid surface becomes large enough to counter balance the surface tension stress.²⁴ When we apply a voltage exceeding 500 volts to increase the electrical stress, the proximity of the drum to the liquid body at the needle tip produces an electrical breakdown, and the jetting initiates and a liquid bridge between needle tip and rotating drum forms. As clear from Equation (5), a higher working voltage is an obvious impediment to forming thinner polymer jets. A relatively larger gap in the jetting initiation procedure without touching demands higher operating voltages to initiate the jetting, which explains why previous NFES experiments failed in producing the thin polymer nanofibers of this study.²⁴ In summary, with higher conductivity of PAN ink, our touching between the liquid body at the tip of the needle and drum are essential to lower the applied voltage and further reduce the diameter for the jetting initiation and the liquid-bridge stabilization.

Further, it is noted in Figure 2 (e) that after jet initiation a larger needle-drum distance (1.85mm) can be achieved due to stable continuous jetting at 500V. In this case, the increase of x in Equation (5) causes a smaller diameter, which corresponds to previous reported results of increasing the spacing to reduce the fiber diameter.²⁵ Instead of controlling x , we suggest that lowering the applied near-field electrospinning voltage is the most effective way to reduce the fiber diameters further.¹² More importantly, minimizing the volume of the fluid body in the ink droplet allows for an already low applied voltage to be further reduced toward ultra-low applied voltages (see below). Here we detail the effect of altering the flow rate on the volume of the fluid body at the tip of the ink droplet and the applied voltage in order to operate a stable continuous jetting at ultra-low voltage and obtain thinner nanofibers. Each flow rate is associated with a minimum voltage where the cone-jet mode is stabilized, and a maximum voltage beyond which the cone-jet is unstable.²⁴ In Figure 3(a~c) we show the jet diameter for different flow rates, internal diameter of the needle and the applied voltage, and it is clear that the effect of the flow rates and voltage on the diameter is dominant. It is noteworthy that in the absence of flow, the lower applied voltage makes it possible to reduce the tangential electric field component, leading to a decrease of the liquid acceleration in Equation (6) and keeping more and more liquid at the tip of the needle in Figure 3(a~c).

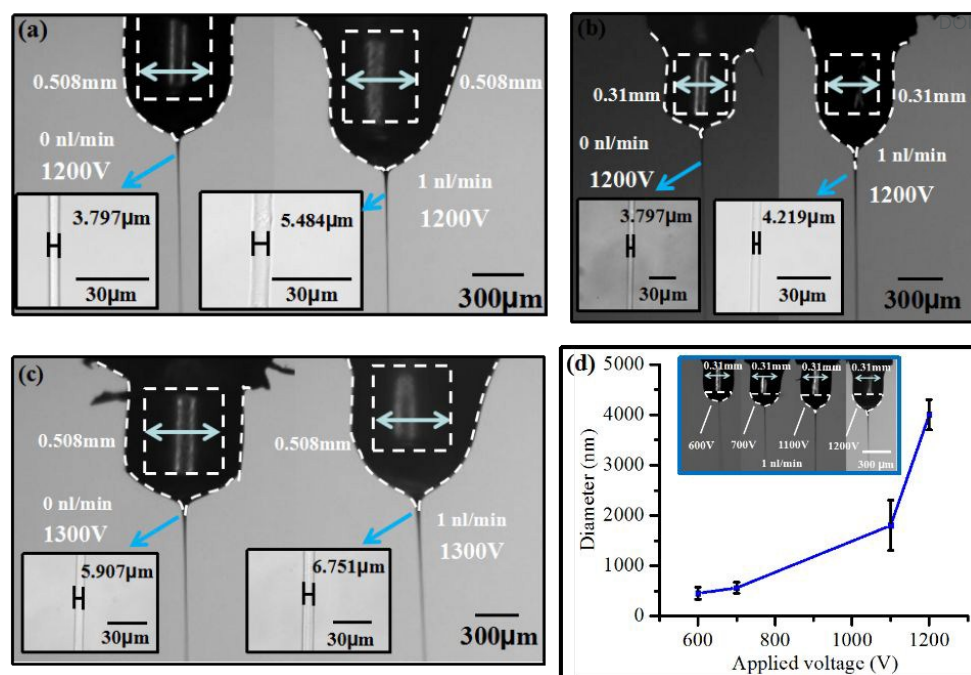


Figure 3. Varying the volume of fluid body in the ink droplet during jetting. (a-c) Effect of the flow velocity on the volume of the fluid body. (d) The effect of the voltage and the diameter on the volume of the fluid body at a fluid flow rate of 1 nl/min.

By reducing the applied voltage from low to ultra-low we were able to obtain the thinnest possible polymer NFES jet achieved today. When, at a flow rate of 1 nl/min, we reduce the voltage from 1200 V to 500V in Figure 3(d) and Figure 2(e) and then reduce the voltage further to below 300V, the liquid bridge connecting the nozzle to the drum disappears. This is expected as the normal electrical stress on the liquid surface is now insufficient to balance the surface tension stress.²⁶ Nevertheless, sufficient normal electrical stress can also be controlled by varying the volume and shape of the fluid body at the top of the needle from a cone to a hemisphere with a small cone tip, as shown in Figure 3(d) and Figure 2(e). Therefore, controlling the volume and shape of the fluid body at the top of the needle by decreasing the flow rate and implementing a porous absorbent paper [see Figure 4(a)] named as extender cap²⁴, allow us to directly control the jetting stability, which provides an effective basis for the ultra-low voltage strategy implementation.

Because of the very low flow rates we work at, the stable cone-jet mode is confined between two boundaries: the upper voltage boundary between the cone-jet and multi-jet modes [see above and Figure 2(f)], and the lower voltage boundary at the stable cone-jet modes [see Figure 4(a)]. The gap between high and low voltage boundaries reduces to zero as the flow rate is increased and a stable cone-jet can only be achieved if the flow rate is sufficiently low. As previously mentioned, there is an interaction between the liquid and the porous absorbent paper, which is maintained after the cone-jet is formed. The porous absorbent paper results in a much broader stability of the cone-jet mode for much higher flow rates. Also, it is observed that the cone-jet formed with the extender cap is much more stable compared to the simple nozzle when both of them operate at the same flow rate.²⁴ Therefore, with a porous absorbent paper as the extender cap in Figure 4(a) and Figure 4(b), it can be concluded that the decreased flow rate that comes with an decreased shear

stress means a decreased minimum voltage for the cone-jet stabilization.

View Article Online
DOI: 10.1039/D0NR00031K

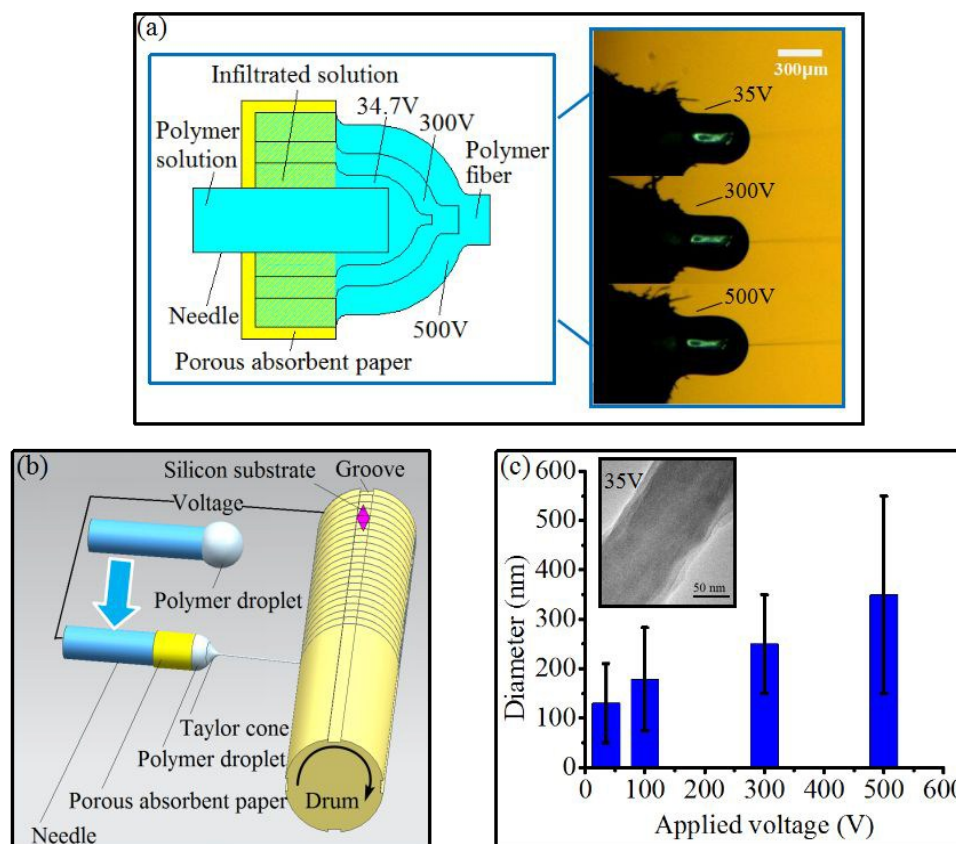


Figure 4. Ultralow-voltage near-field electrospinning effect on the polymer nanofiber diameter. (a) NFES operation at different applied voltages from 500V to 35V (ultra-low voltage). (b), Continuous deposition of polymeric nanofibers onto a silicon substrate on a rotating drum at an ultra-low voltage 35V. (c), Polymer fiber diameter as a function of the applied voltage. Transmission electron micrograph of deposited nano-fibers on microgrid in (b).

Experimentally, we have found though that by introducing a porous absorbent paper band around the needle close to the tip as an extender cap as illustrated in Figures 4(a) and 4 (b) and by reducing the ink flow rate the volume of fluid body near the nozzle is reduced dramatically [see Figure 4(a)] and this allows us to lower the operating voltage much further. The paper strip here plays a somewhat similar role to that of an extender cap as described by Morad et al²⁴. In the “extender cap” configuration introduced here the electric field intensity on the liquid-air interface is substantially higher than that of the simple nozzle at the same voltage since the liquid layer is much thinner, resulting in a smaller working voltage.²⁴ Then based on Equation (5) we expect that this reduction of the working voltage causes a decrease in the jetting diameter. The effect of the applied voltage on the thickness of the nanofibers reveals indeed a decrease in fiber average diameter with decreasing voltage as shown in Figure 4(c). In this configuration, continuous jetting at an ultra-low applied voltage of 35 V is possible and the average diameter of the polymeric fiber may be as low as 50nm.

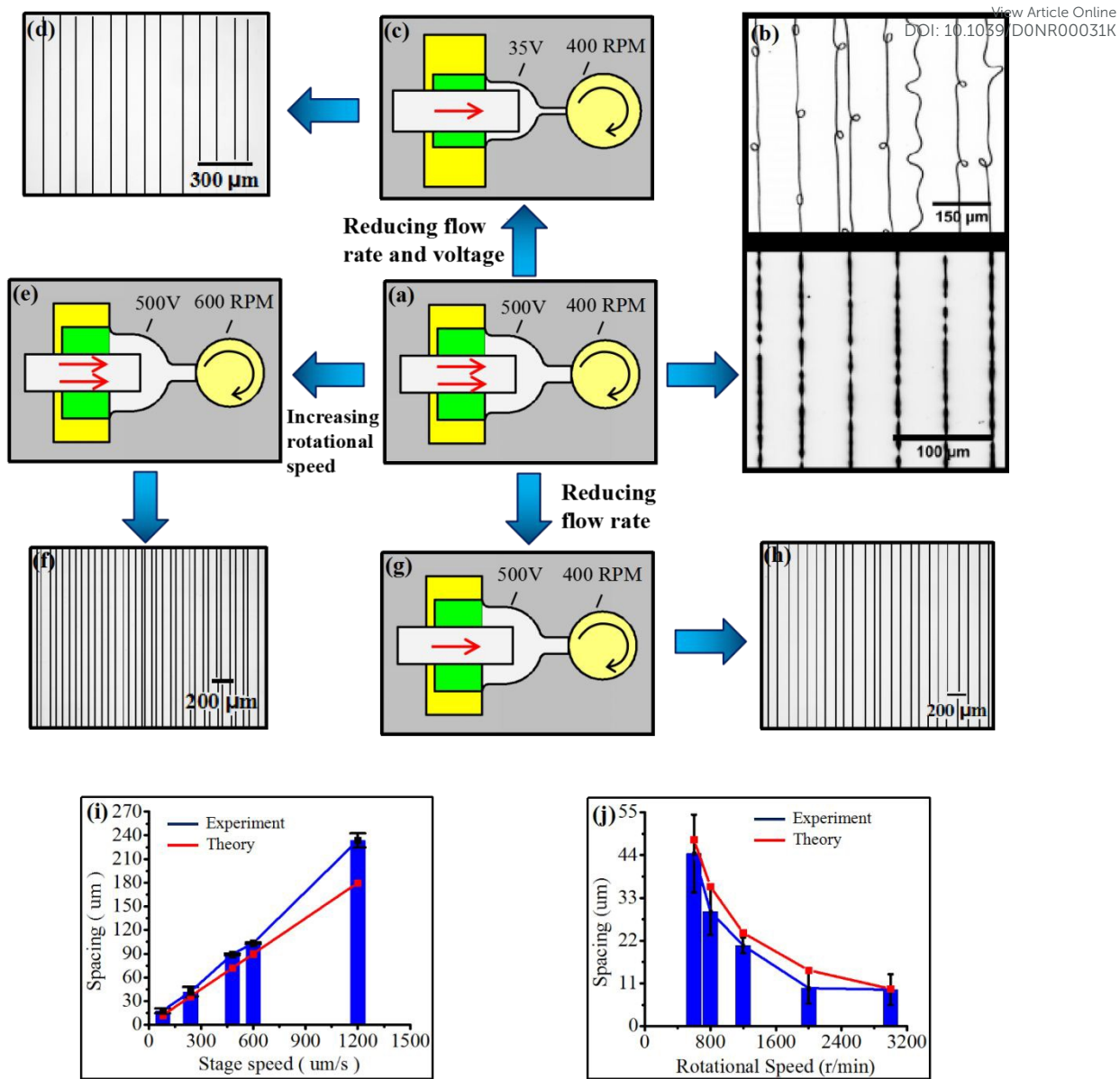


Figure 5. Rapid patterning of electrospun polymer nanofibers over large surface areas. (a-b), Deposition pattern of nanofibers formed by low-voltage NFES of 9% PAN at 500V and at 400 RPM. The beaded and curved patterns are believed to occur due to the bending instability in the jet. (c-h), Straight alignment pattern of nanofibers formed by lowering the applied voltage in (a) to 35V, increasing the rotating speed up to 600 RPM, and reducing the flow rate to almost zero. (i, h) Highly uniform spacing between polymer nanofibers in an array by varying the linear stage speed and rotational speed, respectively, at 35V.

Current state-of-the-art electrospinning methods for aligned polymeric nanofibers deposition suffer from various deficiencies, including curving and beading of the fibers as seen in Figure 5b.²⁷ These phenomena are eliminated when operating at the lowest possible voltages (200V) and when using a viscoelastic ink formulation that prevents fiber breakage upon mechanical pulling.¹² These deficiencies in the deposition pattern are related to the relative velocity between the jetting velocity from the nozzle and the linear velocity on the drum surface. As the applied voltage is reduced to 35 volts in Figure 5(c), the jetting velocity of the formed nanofiber is found to become

smaller in Equation (6), resulting in a large relative velocity between the jetting velocity at droplet and the linear velocity on the drum surface. Further, as shown in Figure 5(d), the linear velocity on the surface of the drum can straighten the entangled fibers and uniformly stretch the fibers with dot-line structure. Once the viscosity and the flow velocity of the pretreated solution decreases, respectively, in Figure 1(d) and Figure 5(g), the corresponding viscous stress will become reduced, which in turn lower the jetting velocity in Equation (6). This result in Figure 5(h) still coincides with that of straight patterned nanofibers. In contrast to lowering the jetting velocity to achieve the straight aligned fibers, the transition of the linear velocity on the drum surface is considered as an alternative to alter the relative velocity. Hence, increasing the linear velocity of the chip on the surface of the drum by increasing the rotational speed of the drum can further stretch the fibers in Figure 5(b) and allow the thin fibers to be arranged in straight patterns on chips mounted on the rotating drum in Figure 5(f). Importantly, the liquid flow velocity inside the needle tube is the key factor for reducing voltage and obtaining defect-free pattern. As a consequence, lowering the viscosity and flow velocity of PAN ink is the most critical for the manufacture of aligned nanofibers at ultra-low voltage.

With defects such as beading and curving of the nanofibers understood and avoided and with the smallest possible fiber diameters achieved with the set-up described here, we are now ready to tackle the challenge of the precise control of the fiber spacing to yield a high-end, manufacturing tool for nanofiber arrays. Impressively, the fiber spacing with using shear force fiber spinning is more uniform than general electrospinning as indicated by the ~ 2 -fold reduction in relative standard deviation.²⁸ Therefore, a rotating drum is introduced to add shear force into our electrospinning system. Although formation and deposition of the single, stable filament from droplet have been well controlled at ultra-low voltage, achieving controlled fiber-to-fiber spacing has to be imperative with the highly advanced automated micropositioning systems. By controlling the programmed linear movement of stage on which needle is fixed, the polymer nanofibers can be aligned and deposited on the substrate with a certain spacing. As shown in Figure 5(i), fiber-to-fiber spacing could be readily tuned with the linear speed of needle. In this set-up, uniform and small fiber-to-fiber spacings d are achieved by controlling the rotating speed ω of a drum and the linear speed v of the nozzle moving along the surface of that drum.²⁸ In this configuration the fiber-to-fiber spacing is given as:

$$d=v/\omega \quad (7)$$

Using ultra-low voltages (35V) and maximizing ω and minimizing the linear speed v results in spacing as small as 8 μm . Below $d = 8 \mu\text{m}$ the spacings become irregular due to such effects as air turbulence, fiber twinning and vibrations. In Figure 5(i) and 5(j) we compare our experimental results with the theory. Regular arrays are achieved as long as ω remained higher than 400 RPM and v above 80 $\mu\text{m/s}$.

Traditional fabrication of carbon nanofibers from PAN relies typically on their stabilization in air at 200-300 $^{\circ}\text{C}$ and their subsequent carbonization in an inert atmosphere at 1000-1500 $^{\circ}\text{C}$, resulting in carbon nanofibers with diameters between 150nm and 500nm.¹⁷ In contrast with traditional protocols, we have found that a lower stabilization temperature and a higher-heating rate (15 $^{\circ}\text{C/min}$ vs 2.5 $^{\circ}\text{C/min}$) allows for a seamless carbonization with superior control of the final nanofiber thickness. When PAN nanofibers are deposited onto a Si substrate equipped with carbon scaffolds as shown in Figure 6(a), they are either in contact with the silicon surface, the carbon surface of the scaffold, or they are suspended between the scaffolds. Using C-MEMS

methods,^{29,30} the carbon scaffolds in Figure 6(a)–6(c) are fabricated by the pyrolysis of patterned high-aspect ratio SU-8 structures in a nitrogen environment. When stabilizing the PAN fibers at 260 °C, the suspended fibers shrink and bend as shown in Figure 6(c). This is most likely the result of cyclization and incipient dehydrogenation of the PAN polymer chains causing the polymer to become denser. It is this “stabilization chemistry” that enables the polymer to survive the pyrolysis step.^{13,14} Unfortunately, this does not yet mean that the carbon nanofiber will not break during pyrolysis. Pyrolysis at 1000 °C, leads to radial and longitudinal contraction as well as enhanced tensile strength of the stabilized PAN nanofibers because of the increased carbon content.^{14–16} However, the longitudinal contraction is restricted by the suspending carbon scaffolds, ultimately resulting in the fracture of the suspended carbon nanofibers as shown in Figure 6(d). In the case that no stabilization treatment is applied, the nanofibers during the pyrolysis sag and touch the the silicon substrate at the bottom of the trench, as illustrated in Figure 6(b). Since we start off with thinner polymer nanofibers, the resulting carbon nanofibers in both cases have diameters between 20 and 50 nanometers, which is far thinner than your typical traditional carbon nanofiber diameter.¹⁷

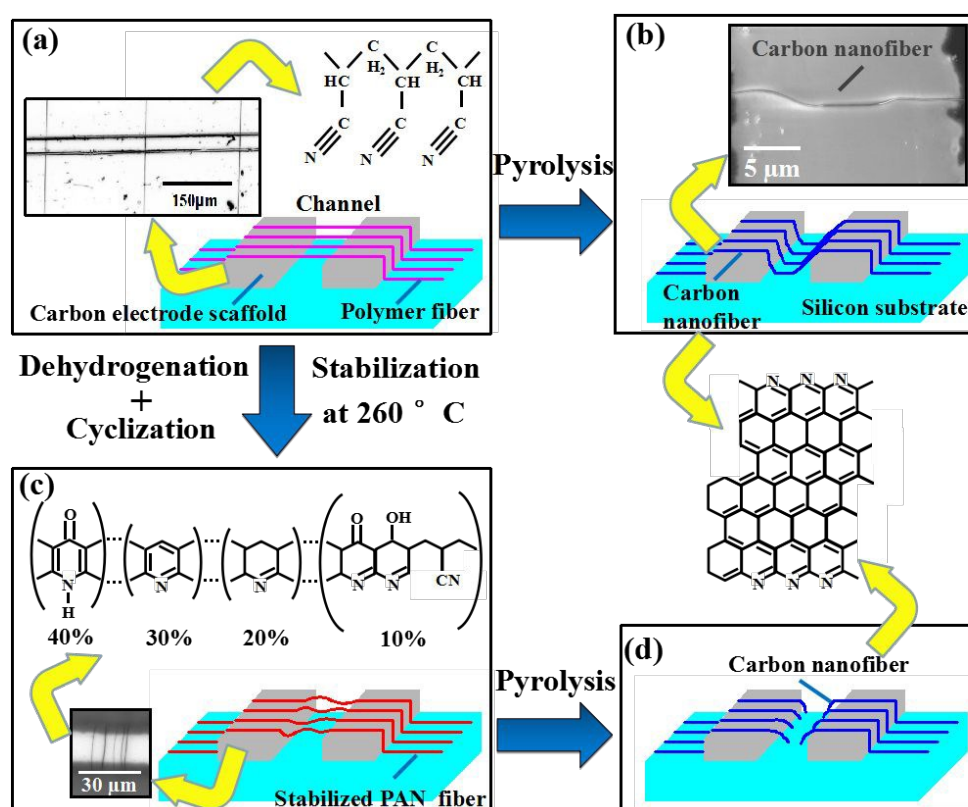


Figure 6. Fabrication of carbon nanofibers from PAN fibers on a Si substrate equipped with carbon scaffolds. The fibers are subjected to different pre-pyrolysis conditions. (a) Aligned polymer nanofibers deposited using ultra-low voltage NFES (35V). (b) Bending and sagging behavior of suspended carbon fibers in the absence of stabilization treatment. (c) Buckled PAN nanofibers stabilized at 260°C. (d) Fractured carbon fibers from the pyrolysis of buckled fibers. Pyrolysis ramp rate is 2.5 °C/min and hold temperature is 1000°C.

From Figure 6 it is clear that stress management is crucial to yield ultrathin fibers that do not break upon pyrolysis. Stabilization at 260 °C causes too much tensile stress resulting in bending while in the absence of stabilization the fibers sag i.e. there is too little tensile stress. By adopting

115°C as the stabilization temperature, we were able to maintain straight suspended nanofibers after stabilization. To convert these very thin suspended and stabilized polymer fibers into the thinnest possible carbon fibers we have to induce the maximum amount of weight loss and diameter shrinkage during the stabilization and pyrolysis steps while keeping the PAN pyrolyzable and at the same time avoiding breakage of the suspended fibers. The dilemma is that upon ramping the temperature to carbonization temperatures ($> 800\text{ }^{\circ}\text{C}$) in an inert atmosphere,⁴ the fibers are once again exposed to heating at $260\text{ }^{\circ}\text{C}$, and we know from the results in Figure 6(c) and Figure 6(d) that suspended nanofibers at $260\text{ }^{\circ}\text{C}$ suffer from too dramatic a shrinkage and subsequently do break upon pyrolysis at a ramp rate of $2.5\text{ }^{\circ}\text{C}/\text{min}$ from 260 to $1000\text{ }^{\circ}\text{C}$. We overcame this problem by implementing a faster ramp rate of $15\text{ }^{\circ}\text{C}/\text{min}$ from 115 to $1000\text{ }^{\circ}\text{C}$ in a nitrogen environment. This faster ramp rate reduced the severe shrinkage at 260°C , resulting in the formation of intact large-area ultra-thin suspended carbon fibers as illustrated in Figure 7(a) and 7(b). Figure 7(a) reveals another important mechanism controlling the carbon nanofiber diameter i.e. the nature of the material in contact with the fiber during pyrolysis i.e. Si, carbon or air (in case of suspended fibers). From Figure 7(c), the fiber shrinks to $\sim 150\text{ nm}$ when deposited on Si, to $\sim 17\text{ nm}$ when deposited on carbon and to $\sim 4\text{ nm}$ when freely suspended between the carbon scaffolds. A combination of the effects of surface wetting and thermal expansion coefficients mismatch at the carbon interface contribute to the differing degrees of shrinkage. In the case of a suspended fiber, the increase in accessible surface area for pyrolysis gases to escape decreases the fiber diameter even further. From the images in Figure 7(a) it is also observed that the morphology of the carbon nanofibers differs dramatically depending on the material interfacing the fibers: from a fractured granular structure on a Si substrate, to a uniform and intact structure on carbon scaffold and in air (suspended). With carbon as a substrate, the better matching of the thermal expansion coefficients ensures the intact survival of the carbon nanofiber. Figure 7(d) illustrates the correlation between the PAN fiber thickness and the applied voltage and the carbon fiber diameter derived from those polymer fibers. Clearly, the polymer fibers obtained at the lowest voltages result -upon pyrolysis- in the thinnest carbon fibers.

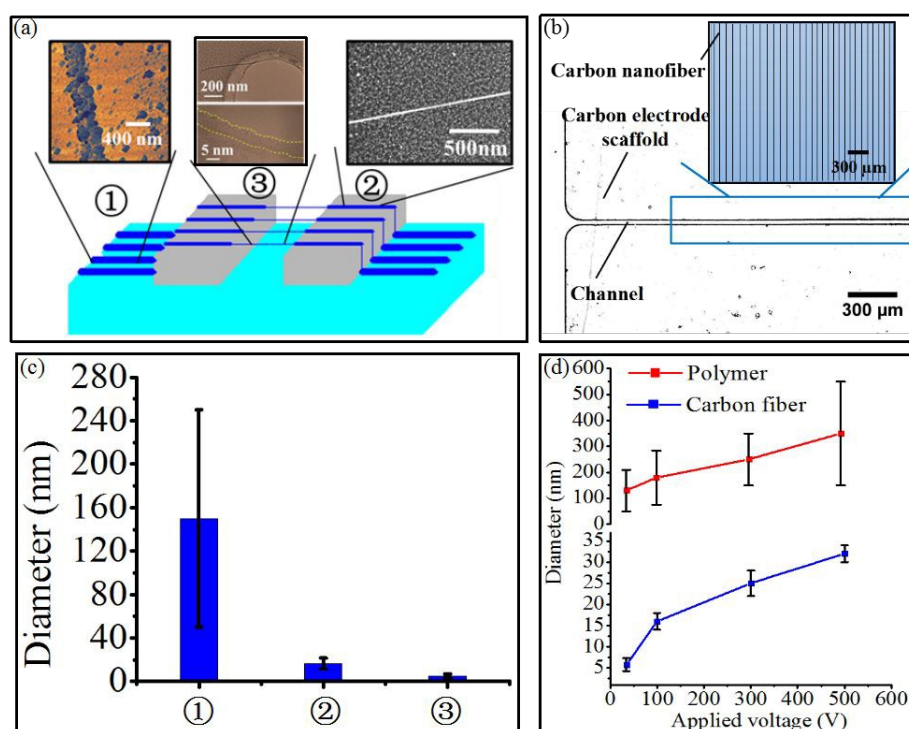


Figure 7 Aligned ultrathin carbon nanofibers on Si, carbon and fibers that are suspended (a). The morphology of the carbon nanofiber obtained by stabilization at 115 °C and pyrolysis at 1000 °C. ①Si: Atomic force microscope (AFM) image of fractured carbon nanofibers on the silicon substrate (diameter ~150 nm). ②Carbon: Scanning electron microscope (SEM) picture of uniform carbon nanofibers on the carbon scaffold (diameter ~17 nm). ③Suspended fibers: Transmission electron microscope (TEM) photograph of suspended carbon nanofibers (diameter ~4 nm). (b) Straight alignment of large-area suspended ultrathin carbon nanofibers. (c) Diameters of carbon nanofibers on Si, carbon and suspended. (d) Correlation between fiber thickness and the applied voltage for PAN polymer and the carbon fiber diameter derived from those polymer fibers.

Based on the above described nanofibers manufacturing procedures, the conversion of PAN polymer fibers to carbon fibers causes the fibers to undergo a dramatic shrinkage of up to 4900% (e.g. from a ~245nm polymer fiber to a ~5nm carbon fiber). In this work we have demonstrated the scalability of a novel ultra-thin nanofibers fabrication process for the fabrication of large-area ultra-thin carbon nanofiber arrays with small inter-fiber spacing [see Figure 7(b)]. This regular arraying was made possible by the simultaneous control of the linear speed of the spinneret and the rotational speed of the collector. Using this configuration, in one application, we demonstrate aligned ultra-thin carbon fibers freely suspended and in good ohmic contact with carbon scaffolds on a silicon substrate. It was the development of a PAN/DMF ink with higher conductivity and lower viscosity that made it not only possible to trigger the jetting in a touch and retract scheme of altering the shape of liquid body at the tip of the needle but also to maintain a continuous jet at ultra-low voltages. More importantly, minimizing the volume of the fluid body in the ink droplet allows for an already low applied voltage to be further reduced toward ultra-low applied voltages. The following pyrolysis converts these polymer nanofiber into ultra thin carbon nanofibers with the available pre-treatment made by using low temperature (115 °C) stabilization and selecting carbon as a scaffold material. Moreover, the ability to achieve scalable patterning precision for ultra-thin carbon nanofibers is conveniently effected through stage speed or rotating speed manipulation. Compared to carbon mats and carbon films, the separated carbon nanofibers herein are benefit to study the signal-to-noise ratio³¹. Meanwhile ultra-thin carbon nanofibers provide more perspective on the potential applications for high-rate supercapacitors³², absorption-dominated electromagnetic interference shielding³³, capacitive deionization³⁴ and electrocatalytic performance³⁵.

ACKNOWLEDGMENT

This research was supported by National Natural Science Foundation of China (51875084). The support provided by China Scholarship Council (CSC) during a visit of Jufeng Deng to the University of California, Irvine is acknowledged.

REFERENCES

- (1) A. Babapoor, M. Azizi, G. Karimi, *Applied Thermal Engineering* 2015, 82, 281-290.
- (2) K. Yu, P. H. Shi, J. C. Fan, Y. L. Min, Q. J. Xu, *J Nanopart Res* 2019, 21, 230.
- (3) S. Manzetti, F. Enrichi, *Adv. Manuf.* 2017, 5, 105-119.

- (4) S. N. Arshad, M. Naraghi, I. Chasiotis, *Carbon* 2011, 49, 1710.
- (5) S. C. Sharma, H. Katepalli, A. Sharma, M. Madou, *Carbon* 2011, 49, 1727-1732.
- (6) J. L. Rife, P. Kung, R. J. Hooper, J. Allen, G. B. Thompson, *Carbon* 2020, 162, 95-105.
- (7) D. Lei, K. Devarayan, M. K. Seo, Y. G. Kim, B. S. Kim, *Materials Letters* 2015, 154, 173-176.
- (8) H. Ashrafi, M. Bazli, A. V. Oskouei, *Construction and Building Materials* 2017, 134, 507-519.
- (9) Y. Hyun, E. S. Park, K. Mees, H. S. Park, M. W. Porada, C. S. Lee, *Journal of Nanoscience and Nanotechnology* 2015, 15, 7293-7304.
- (10) V. I. Merkulov, D. H. Lowndes, Y. Y. Wei, G. Eres, E. Voelkl, *Appl. Phys. Lett.*, 2000, 76, 3555.
- (11) D. Li, G. Ouyang, J. T. McCann, Y. N. Xia, *Nano Lett.* 2005, 5, 913-916.
- (12) G. S. Bisht, G. Canton, A. Mirsepassi, L. Kulinsky, S. Oh, R. D. Dunn, J. M. Madou, *Nano Lett.* 2011, 11, 1831-1837.
- (13) N. Hameed, J. Sharp, S. Nunna, C. Creighton, K. Magniez, P. Jyotishkumar, N. V. Salim, B. Fox, *Polymer Degradation and Stability* 2016, 128, 39-45.
- (14) J. Liu, S. Xiao, Z. Shen, L. Xu, L. Zhang, J. Peng, *Polymer Degradation and Stability* 2018, 150, 86-91.
- (15) H. Khayyam, R. N. Jazar, S. Nunna, G. Golkarnarenji, K. Badii, S. M. Fakhrhoseini, S. Kumar, M. Naebe, *Progress in Materials Science* 2020, 107, 100575.
- (16) R. Zhao, P. Sun, R. Liu, Z. Ding, X. Li, X. Liu, X. Zhao, Z. Gao, *Applied Surface Science* 2018, 433, 321-328.
- (17) M. Inagaki, Y. Yang, F. Y. Kang, *Adv. Mater.* 2012, 24, 2547-2566.
- (18) J. Bauer, A. Schroer, R. Schwaiger, O. Kraft, *Nature Materials* 2016, 15, 438-443.
- (19) H. Yu, J. Guo, S. Q. Zhu, Y. G. Li, Q. H. Zhang, M. F. Zhu, *Materials Letters* 2012, 74, 247-249.
- (20) E. Frank, L. M. Steudle, D. Ingildeev, J. M. Spörl, M. R. Buchmeiser, *Angew. Chem. Int. Ed.* 2014, 53, 5262-5298.
- (21) Y. Eom, Y. Park, Y. M. Jung, B. C. Kim, *Polymer* 2017, 108, 193-205.
- (22) A. Smeets, C. Clasen, G. V. den Mooter, *European Journal of Pharmaceutics and Biopharmaceutics* 2017, 119, 114-124.
- (23) Moses M. Hohman, Michael Shin, Gregory Rutledge, and Michael P. Brenner, *Physics of Fluids*, 2001, 13, 2221-2236.
- (24) M. R. Morad, A. Rajabi, M. Razavi, S. R. Pejman Sereshkeh, *Scientific Reports* 2016, 6, 38509.
- (25) Wang, D. Z.; Zhao, X. J.; Lin, Y. G.; Liang, J. S.; Ren, T. Q.; Liu, Z. H.; Li, J. Y. *Nanoscale*, 2018, 10, 9867-9879.
- (26) M. Yu, K. H. Ahn, S. J. Lee, *Materials and Design* 2016, 89, 109-115.
- (27) X. X. He, J. Zheng, G. F. Yu, M. H. You, M. Yu, X. Ning, Y. Z. Long, *J. Phys. Chem. C* 2017, 121, 8663-8678.
- (28) A. C. Dotivala, K. P. Puthuveetil, C. Tang, *Polymers*, 2019, 11, 294.
- (29) B. Pramanick, M. V. Pinon, A. T. Castro, S. O. M. Chapaa, M. Madou, *Materials Today Proceedings* 2018, 5, 9669-9682.
- (30) R. Natu, M. Islam, J. Gilmore, R. M. Duarte, *Journal of Analytical and Applied Pyrolysis*

2018, 131, 17-27.

View Article Online
DOI: 10.1039/D0NR00031K

- (31) S. Siddiqui, P. U. Arumugam, H. Chen, J. Li, M. Meyyappan, *ACS Nano* 2010, 4, 955-961.
- (32) W. M. Chang, C. C. Wang, C. Y. Chen, *Electrochimica Acta* 2019, 296, 268-275.
- (33) D. Xing, L. Lu, W. Tang, Y. Xie, Y. Tang, *Materials Letters* 2017, 207, 165-168.
- (34) Y. Liu, T. Lu, Z. Sun, D. H. C. Chua, L. Pan, *J. Mater. Chem. A* 2015, 3, 8693-8700.
- (35) M. Weber, N. Tuleushova, J. Zgheib, C. Lamboux, et al., *Applied Catalysis B: Environmental* 2019, 257, 117917.